11TH INTERNATIONAL ERCOFTAC SYMPOSIUM ON ENGINEERING TURBULENCE MODELLING AND MEASUREMENT
SEPTEMBER 21-23, 2016, PALERMO, ITALY

EXPERIMENTAL AND NUMERICAL INVESTIGATION OF ACTIVE FLOW CONTROL ON A GENERIC TRUCK CABIN

Guglielmo Minelli[1], Erwin Adi Hartono[1], Siniša Krajnović[1], Valery Chernoray[1],
Linus Hjelm[2], Branislav Basara[3]
[1] *Chalmers University of Technology, Gothenburg, Sweden*
[2] *Volvo Trucks AB, Gothenburg, Sweden*
[3] *Advanced Simulation Technologies, AVL List GmbH, Hans-List-Platz 1, 8020 Graz*

Abstract This work presents the achievement in drag reduction by use of Active Flow Control (AFC) on a generic bluff body. The model consists of a simplified truck cabin, characterized by sharp edge separation on top and bottom edges and pressure induced separation on the rounded vertical front corner. The pressure induced separation reproduces the flow separation occurring at the front A-pillar of a real truck. Hybrid Partially Averaged Navier-Stokes (PANS) simulations are compared with wind tunnel experiments. The Reynolds number for both simulations and experiments is $Re = 5 \times 10^5$ based on the inlet velocity U_∞ and the width of the model $W = 0.4$ m. A validation of the hybrid CFD model on two flow configurations is followed by a CFD study on the optimal actuation frequency able to minimize the aerodynamic drag. PANS accurately predicts the flow field measured in experiments and a notable drag reduction by means of AFC is observed in a numerical study.

INTRODUCTION

The flow impinging the front window of a truck cabin separates at the A-pillar, Fig. 1a. The recirculation bubble not only creates drag that deteriorates the performance of the entire truck, but also noise and soiling affecting the comfort of the driver. Introduction of an Active Flow Control (AFC) (violet arrows in Fig. 1b) enables reduction and suppression of the recirculation bubble benefiting the overall performance, Fig 1b.

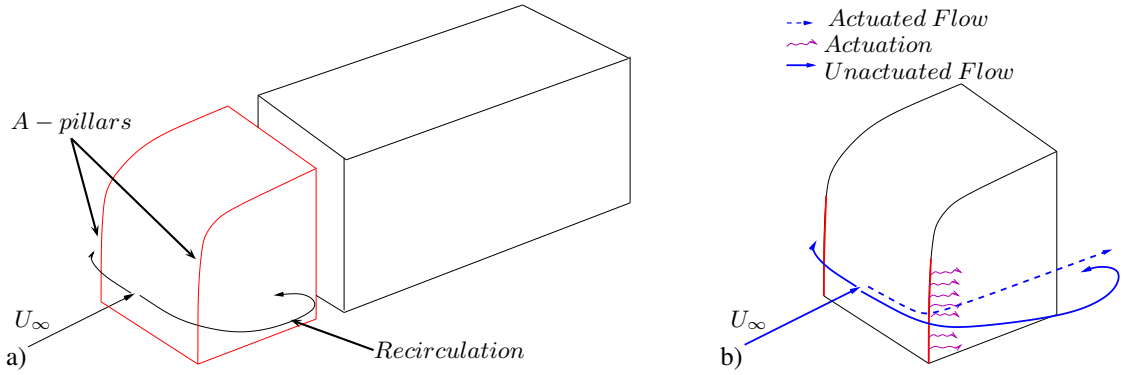

Figure 1. a) the natural behavior of the flow. b) the actuation and its effect

The AFC technique was employed effectively in bluff body studies [1, 2], and reviews of this technique are provided by Gad-el-Hak [3] and Brunton et al. [4]. In [5], the actuation of the flow field around an A-pillar was studied numerically, where interesting results were found on the nature of the front separation and its suppression. However, many aspects such as the influence of the Reynolds number, 3-D effects and the actual feasibility of the actuation in a real case need to be investigated. Thus, experiments and hybrid unsteady numerical simulations are conducted to study the flow around a simplified truck cabin. The Partially Averaged Navier-Stokes (PANS) method is used in this work. PANS was already proven to be effective for different bluff body flows [6–8], but its limits and potential must be investigated more deeply. This paper reports a validation study on the PANS method and the investigation of the separation mechanism's nature and its control, achieving the following goals:

- PANS simulations are validated with experiments for two different flow configurations, at two yaw angles.
- The unactuated flow PANS simulations have been post processed by means of modal decomposition POD and FFT, investigating the nature of the separation mechanism.

- An optimal actuation frequency is found.

NUMERICAL DETAILS

The computational domain is described by Fig. 2 and Tab. 1. All the dimensions are scaled with the model width $W = 0.4m$.

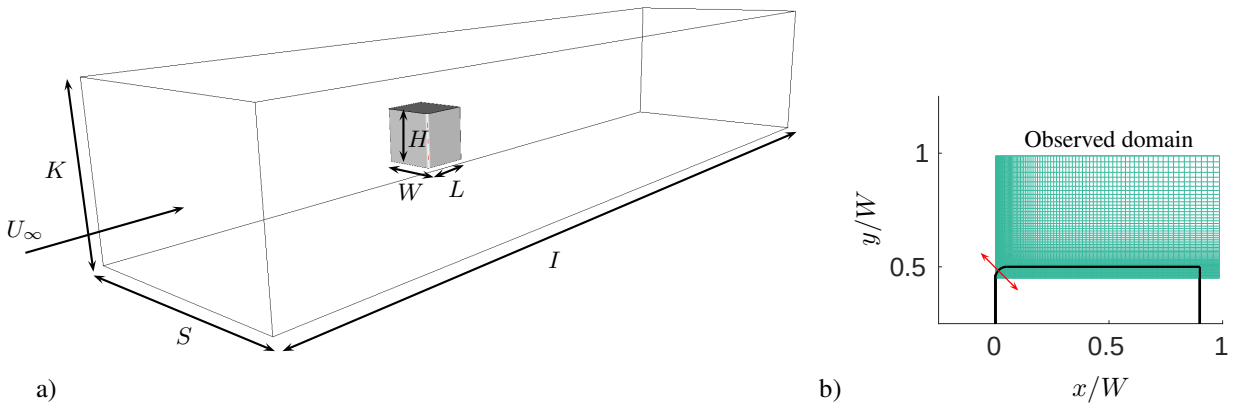

Figure 2. a) The numerical domain. b) Top view of the model and the observed domain. The red arrows indicate the position of the actuation slot and the direction of blown and sucked air through it.

Table 1. Dimension of the numerical domain scaled by the model width $W = 0.4$ m. R is the non-dimensional radius of the rounded corners.

H	L	I	K	S	R
1	0.9	17.5	3	4.5	0.05

A homogeneous Neumann boundary condition is applied at the outlet. The surfaces of the body and the wind tunnel walls are treated as no slip walls. A time varying velocity $U_{afc} = 0.26U_{inf}\sin(t2\pi f_a)$, where f_a is the actuation frequency, is set at the actuation slot. The actuation is highlighted by red arrows in Fig. 2b). A finite grid plane, placed at $z = H/2$ (the coordinate system and the origin is given in Fig. 4), is used to sample snapshots of the flow field, Fig. 2b).
The governing flow equations used in this work are the incompressible partially averaged Naviers-Stokes (PANS) equations [9].

$$\frac{\partial U_i}{\partial x} = 0 \tag{1}$$

$$\frac{\partial U_i}{\partial t} + U_j\frac{\partial U_i}{\partial x_j} = -\frac{1}{\rho}\frac{\partial p}{\partial x_i} + \frac{\partial}{\partial x_j}\left(\nu\frac{\partial U_i}{\partial x_j} + \tau(V_i, V_j)\right) \tag{2}$$

where $\tau(V_i, V_j)$ is the generalized second moment [10] and represents the effect of the unresolved scales on the resolved field. The Bousinnesq assumption is now invoked to model the second moment:

$$\tau(V_i, V_j) = -2\nu_u S_{ij} + \frac{2}{3}k_u\delta_{ij}. \tag{3}$$

Here k_u is the unresolved kinetic energy, $S_{ij} = \frac{1}{2}(\partial U_i/\partial x_j + \partial U_j/\partial x_i)$ is the resolved stress tensor, and $\nu_u = C_\mu\zeta_u k_u^2/\varepsilon_u$ is the viscosity of the unresolved scales where $\zeta = \overline{v_u^2}/k_u$ is the velocity scale ratio of the unresolved velocity scale $\overline{v_u^2}$ and k_u. $\overline{v_u^2}$ refers to the normal fluctuating component of the velocity field to any no-slip boundary. At this stage three transport equations for $k_u - \varepsilon_u - \zeta_u$ and a Poisson equation for the elliptic relaxation function of the unresolved velocity scales are necessary to close the model. Thus the complete PANS $k-\varepsilon-\zeta-f$ model is given

by the following set of equations:

$$\begin{aligned}
&\frac{\partial k_u}{\partial t} + U_j \partial k_u \partial x_j = P_u - \varepsilon_u + \frac{\partial}{\partial x_j}\left(\frac{\nu_u}{\sigma_{k_u}}\frac{\partial k_u}{\partial x_j}\right)\\
&\frac{\partial \varepsilon_u}{\partial t} + U_j \partial \varepsilon_u \partial x_j = C_{\varepsilon 1} P_u \frac{\varepsilon_u}{k_u} - C^*_{\varepsilon 2}\frac{\varepsilon_u^2}{k_u} + \frac{\partial}{\partial x_j}\left(\frac{\nu_u}{\sigma_{\varepsilon_u}}\frac{\partial \varepsilon_u}{\partial x_j}\right)\\
&\frac{\partial \zeta_u}{\partial t} + U_j \partial \zeta_u \partial x_j = f_u - P_u\frac{\zeta_u}{k_u} + \frac{\zeta_u}{k_u}\varepsilon_u(1-f_k) + \frac{\partial}{\partial x_j}\left(\frac{\nu_u}{\sigma_{\zeta_u}}\frac{\partial \zeta_u}{\partial x_j}\right)\\
&L_u^2\nabla^2 f_u - f_u = \frac{1}{T_u}\left(c_1 + c_2\frac{P_u}{\varepsilon_u}\right)\left(\zeta_u - \frac{2}{3}\right).
\end{aligned} \tag{4}$$

$\nu_u = C_\mu \zeta_u \frac{k_u^2}{\varepsilon_u}$ is the unresolved turbulent viscosity. $P_u = -\tau(V_i, V_j)\frac{\partial U_i}{\partial x_j}$ is the production of the unresolved turbulent kinetic energy and is closed by the Bousinnesq assumption, Eq. 3. The coefficients $C^*_{\varepsilon 2}$ and $C_{\varepsilon 1}$ are defined as:

$$C^*_{\varepsilon 2} = C_{\varepsilon 1} + f_k(C_{\varepsilon 2} - C_{\varepsilon 1}); \qquad C_{\varepsilon 1} = 1.4\left(1 + \frac{0.045}{\sqrt{\zeta_u}}\right).$$

$\sigma_{k_u} = \sigma_k \frac{f_k^2}{f_\varepsilon}$ and $\sigma_{\varepsilon_u} = \sigma_\varepsilon \frac{f_k^2}{f_\varepsilon}$ are the counterpart of the unresolved kinetic energy and dissipation, respectively. In this way f_k and f_ε contribute to changing the turbulent transport Prandtl number contributing to the decrease of the unresolved eddy viscosity [11]. The constants appearing in 4 are:

$$C_\mu = 0.22; \quad C_{\varepsilon 2} = 1.9; \quad c_1 = 0.4; \quad c_2 = 0.65; \quad \sigma_k = 1; \quad \sigma_\varepsilon = 1.3; \quad \sigma_{\zeta_u} = 1.2.$$

L_u and T_u are the length and time scales defined by using the unresolved kinetic energy:

$$L_u = \max\left[\frac{k_u}{\varepsilon}, C_\tau\left(\frac{\nu}{\varepsilon}\right)^{1/2}\right]; \quad T_u = C_L \max\left[\frac{k_u^{3/2}}{\varepsilon}, C_\eta\left(\frac{\nu^3}{\varepsilon}\right)^{1/4}\right]$$

where

$$C_\tau = 6; \;\; C_L = 0.36; \;\; C_\eta = 85.$$

A more detailed explanation of the construction of the equations is given in [12, 13]. Parameters f_k and f_ε are the key factors that make the model act dynamically. f_k and f_ε are the ratios between resolved to total kinetic energy and dissipation, respectively, and they can assume values between 1 and 0 according to the selected cut-off. The dynamic parameter was proposed as the ratio between the geometric averaged grid cell dimension, $\Delta = (\Delta_x\Delta_y\Delta_z)^{1/3}$, and the Taylor scale of turbulence, $\Lambda = \frac{(k_u + k_{res})^{3/2}}{\varepsilon}$ [14]:

$$f_k(x,t) = \frac{1}{\sqrt{C_\mu}}\left(\frac{\Delta}{\Lambda}\right)^{2/3}. \tag{5}$$

The PANS equations are discretized with the commercial finite volume CFD solver AVL FIRE [15]. AVL FIRE is based on the cell-centered finite volume approach. The PANS are solved using a collocated grid arrangement. Convective fluxes are approximated by a second-order upwind scheme called AVL-SMART in AVL Fire [15]. The time marching procedure is done using the implicit second-order accurate three-time level scheme. The well known SIMPLE algorithm is used to update pressure and velocity fields in order to satisfy the continuity equation.

THE EXPERIMENTS

Experiments are carried out in a closed circuit wind tunnel at Chalmers University with test section dimensions of $3.00 \times 1.80 \times 1.25$ m^3 and a speed range of 0-60 m/s. Figure 3a represents a CAD model of the wind tunnel test section and the model in place. Figure 3b shows a real picture of the model in the wind tunnel. The oncoming flow turbulence level was within 0.5%.

a) 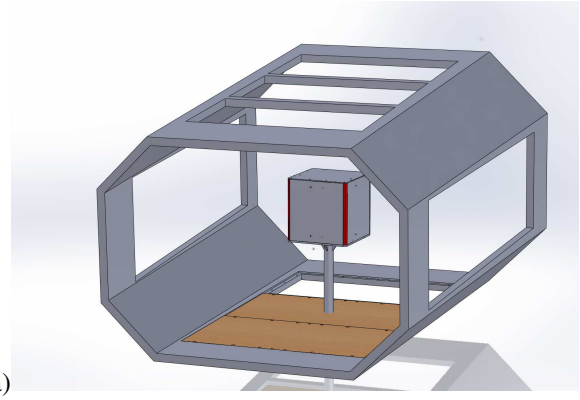 b) 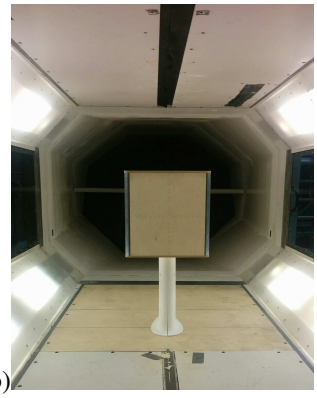

Figure 3. The experimental model. a) CAD overview of the model and wind tunnel test section. b) The model placed in the Chalmers' wind tunnel.

The experimental model is equipped with arrays of pressure taps distributed along the front (A), windward (B), leeward (C) and base (D) faces as shown in Fig. 4. Faces B and D are termed windward and leeward respectively, also in the $\beta = 0°$ con for simplicity. Every face is given a letter from A to D. Each face was equipped with a horizontal and vertical array of pressure taps (dashed blue line in Fig. 4) for evaluation of the coefficient of pressure, C_p, during the experiments. The pressure profiles of two configurations at yaw angles $\beta = 0°$ and $\beta = 10°$ have been measured and compared with numerical simulations. The pressure system (NetScanner^{TM} model 9116) has an accuracy of $\pm 0.2Pa$. The sampling frequency used in the experiments was $1000Hz$, and the pressure signals were averaged over a period of $2s$. The agreement of the results is discussed in the next section.

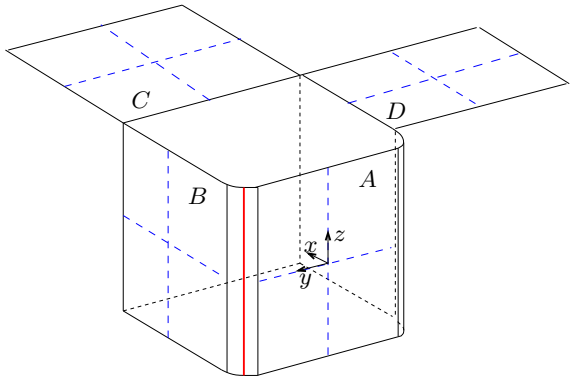

Figure 4. The model of a generic truck cabin. (------) pressure taps distribution. (——), position of the actuation slot. A front face, B windward face, C base face, D leeward face.

RESULTS

This section is divided into two parts. A validation of PANS is first presented. Secondly, PANS are used to simulate the effect of the actuation on the flow around the A-pillar of a generic truck cabin.

PANS accuracy and validation

PANS method is evaluated on two different flow cases. Both the first case at yaw angle $\beta = 0°$ and the second at $\beta = 10°$ give good agreement between experiments and simulations. The meshes employed are relatively coarse for the considered Reynolds number, Tab. 2. A well resolved Large Eddy Simulation (LES) would require a resolution of $\Delta l^+_{max} < 30$ and $\Delta s^+_{max} < 100$ in the spanwise and streamwise directions, respectively [16]. Using meshes far from being sufficient for a well resolved LES, Tab. 2, PANS gives results in good agreement with experiments, yet capturing the dynamics of the flow structures. The details of the meshes are summarized in Tab. 2.

Table 2. Details of the computational grids

Case	Medium grid	Coarse grid
Number of cells	12 millions	6 millions
y^+_{mean}	< 0.5	< 0.5
Δl^+_{max}	< 300	< 450
Δs^+_{max}	< 300	< 450
CFL	< 1	< 1

The $\beta = 0°$ configuration has been imulated on both medium and coarse meshes. The $\beta = 10°$ configuration has been simulated only on the medium grid.

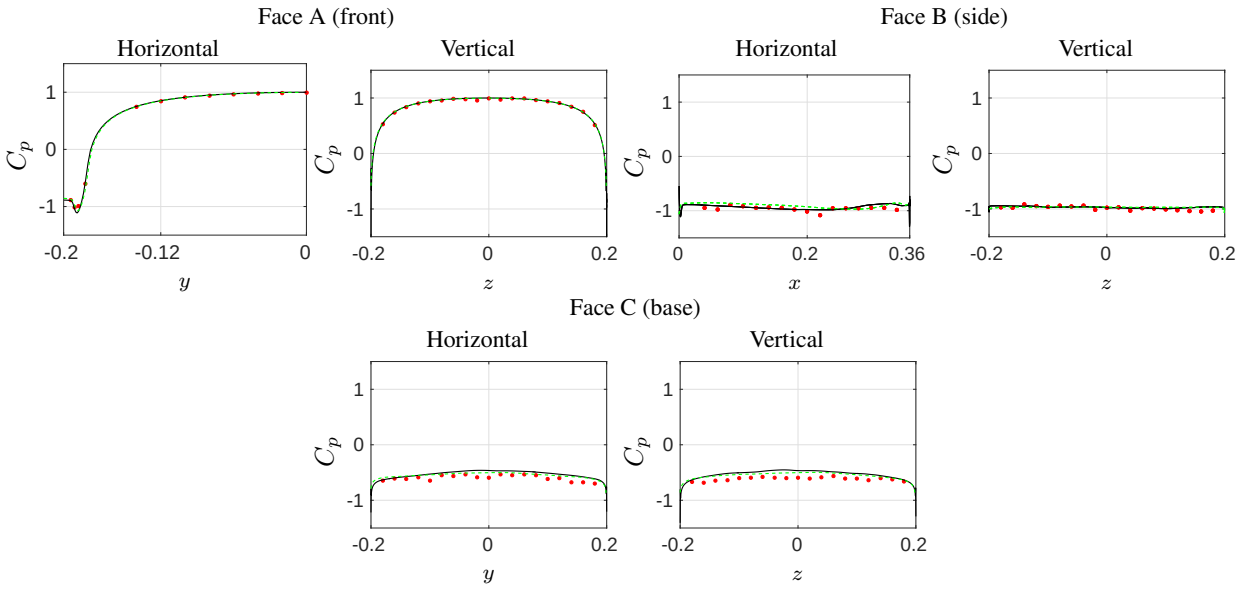

Figure 5. C_p profiles comparison, $\beta = 0°$. (——) PANS medium mesh, (------) PANS coarse mesh, (• • • •) experiments. A front face, B windward face, C base face. Notation and coordinates refers to Fig. 4.

A small discrepancy between experiments and CFD is found in the prediction of the windward face flow. The flow in this area is more complicated as compared to other faces. It includes separation, reattachment and strong 3-D effects coming from the top and bottom separations. The shape of the vertical and horizontal profiles of face B, Fig. 6, is conserved but shows an offset from the experimental data. On the other hand, the front face flow (attached flow), the leeward and the base face flows (completely separated flow) are predicted accordingly to the experimental data, for both yaw configurations and for the coarse mesh computed for $\beta = 0°$ yaw.

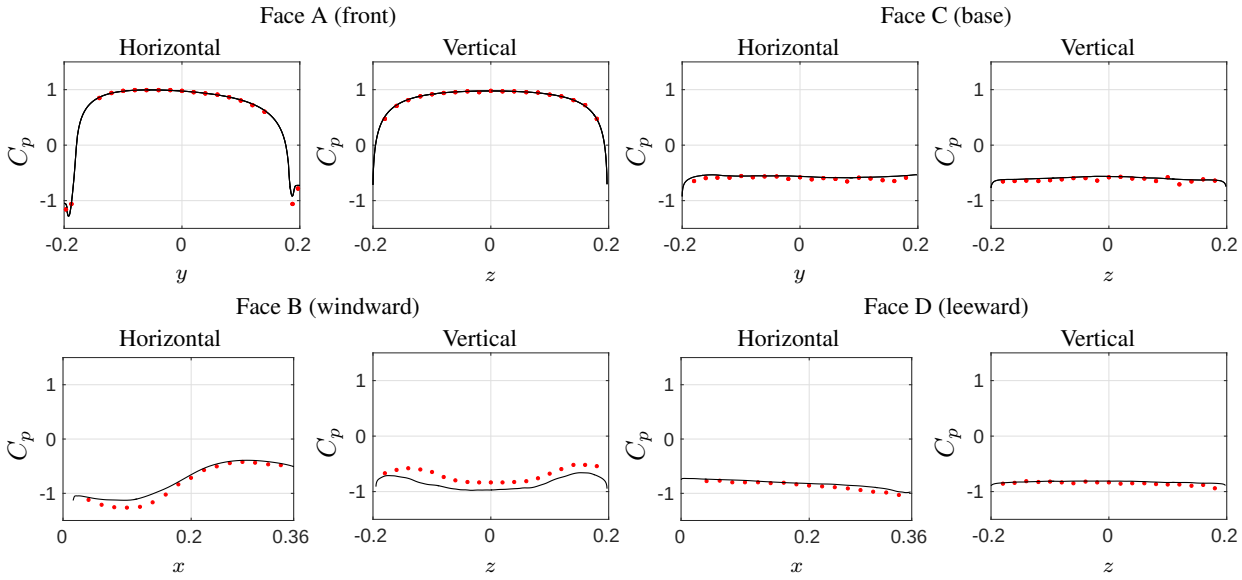

Figure 6. C_p profiles comparison, $\beta = 0°$. (——) PANS medium mesh, (· · · ·) experiments. A front face, B windward face, C base face, D leeward face. Notation and coordinates refer to Fig. 4.

Actuation study

The medium mesh has been employed to study the actuation of the flow. The unactuated flow has been post-processed with Proper Orthogonal Decomposition (POD) [17] and Fast Fourier Transform (FFT) modal analysis. As described in [5], the separated flow of a rounded leading edge is mainly characterized by high-frequency shear layer structures and low-frequency side wake structures. POD and FFT capture these structures and their frequencies, respectively. In particular, the near wake structures are characterized by a normalized frequency $F^+ = fW/U_\infty = 0.4$, while the shear layer structures are characterized by $F^+ = 3.0$, Fig. 7.

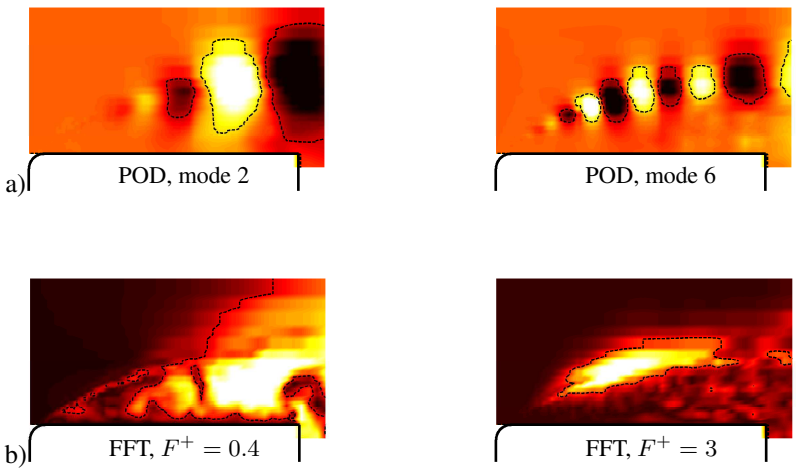

Figure 7. a) Pressure POD mode 2 (left) and mode 6 (right); the colors indicate low (black) and high (white) pressure structures. b) Spatial distribution of $F^+ = 0.4$ (left) and $F^+ = 3$ (right). The colors indicate where each frequency occurs the most (white) and the least (black). Flow from left to right.

Thus, three different actuated cases have been simulated. The near wake frequency, $F^+ = 0.4$, the shear layer frequency, $F^+ = 3$, and a third frequency, $F^+ = 8.3$, have been used to actuate the flow. The actuation cases are denoted $Case1$ (F+=0.4), $Case2$ (F+=3) and $Case3$ (F+=8.3). Evaluating the existence of an optimal control frequency and finding a relation between actuation frequency and unactuated flow structures are of primary importance. Aerodynamic performance and actuation effects are described in Figs. 8, 9, 10.

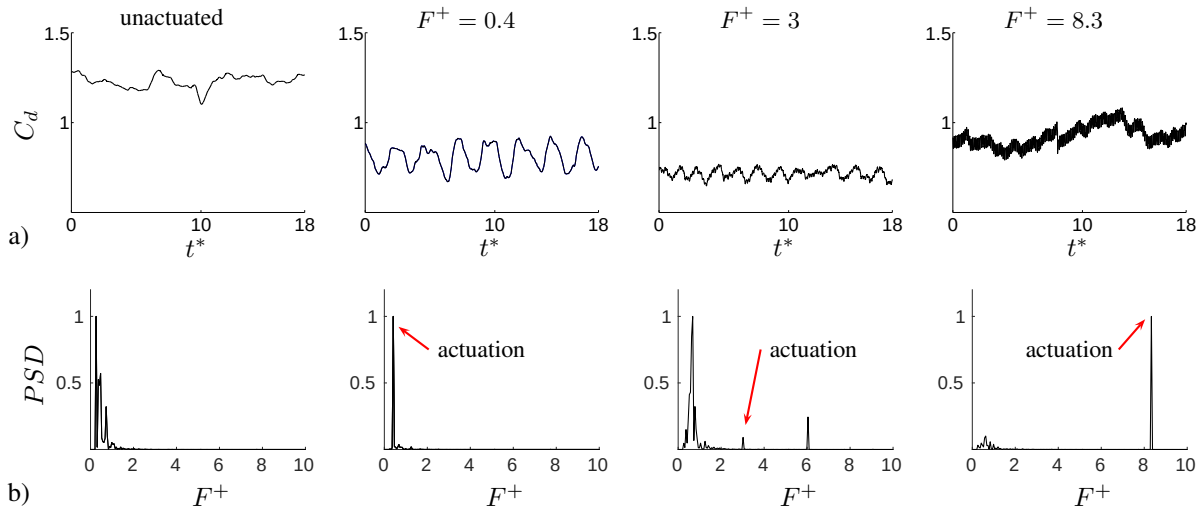

Figure 8. a) C_d time history. b) Power Spectral density of the C_d . From left to right: unactuated flow, actuated at $F^+ = 0.4$, actuated at $F^+ = 3$, actuated at $F^+ = 8.3$. The red arrows indicate the power of the actuation frequency.

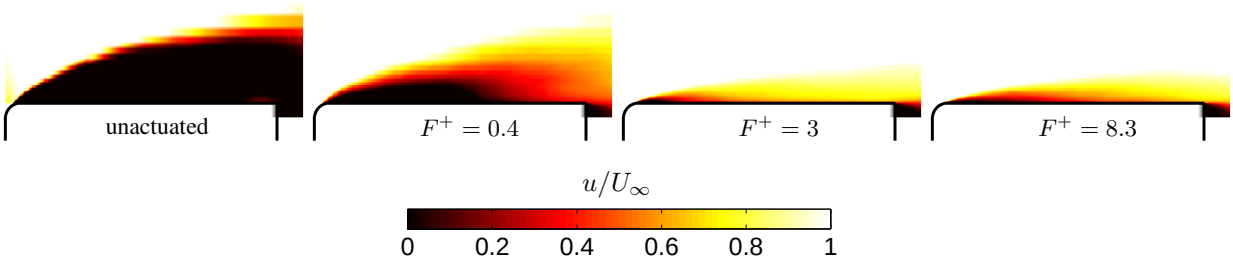

Figure 9. Normalized streamwise velocity component. From left to right: unactuated flow, actuated at $F^+ = 0.4$, actuated at $F^+ = 3$, actuated at $F^+ = 8.3$. The black region represents the reverse flow areas. Flow from left to right.

Figure 8a and 8b show the drag coefficient time history and its Power Spectral Density highlighting the existence of an optimal actuation frequency. $Case1$ shows a high decrease in drag, Fig. 8a, but introduces high induced fluctuations that force the C_d to fluctuate at the actuation frequency. Indeed, the PSD of $Case1$ shows the highest peak at the actuation frequency, Fig. 8b. $Case3$ shows a lower reduction of aerodynamic drag, but in this case the introduced fluctuations are more limited, although they are dominant when considering its PSD, Fig. 8b. $Case2$ shows the optimal case, with a C_d reduction of 50% and limited introduced fluctuations. Hence, its PSD, Fig. 8a, shows that the actuation frequency is not dominant in the drag coefficient. Figure 9 shows the reduction of the recirculation bubble for different actuations. Once again, $Case2$ shows the highest reduction of reverse flow. Nevertheless, $Case3$ shows a similar reduction compared to $Case2$. The higher C_d value, visible in Fig. 8a, is therefore explained by a lower base pressure, as illustrated by Fig. 10.

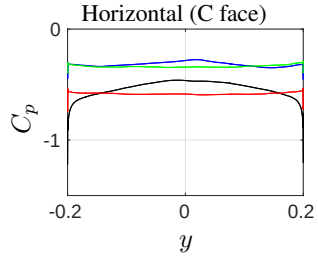

Figure 10. C_p along the horizontal line on the base face (face C). Letters and coordinates refer to Fig. 4. (——) unactuated flow, (——) actuated at $F^+ = 0.4$, (——) actuated at $F^+ = 3$, (——) actuated at $F^+ = 8.3$.

The actuation has a strong effect on the base pressure. $Case3$ (red line) shows a low C_p value along the base, explaining its poorer aerodynamic performance when compared to $Case2$ (green line). On the other hand, the C_p value of $Case1$ (blue line) is similar to the one in $Case2$, but, in this case, the aerodynamic performance is negatively affected by the larger recirculation bubble occurring on the side of the model.

CONCLUSIONS

PANS simulations and experiments at $Re = 5 \times 10^5$ were conducted to analyze the accuracy of PANS and to investigate the actuation of the flow field around a generic truck cabin. The following goals have been achieved:

- PANS has been compared with experiments at two yaw configurations ($\beta = 0^\circ$ and $\beta = 10^\circ$). Results show good agreement, highlighting the accuracy of PANS in calculating 3-D unsteady bluff body flows.
- The POD and FFT analyses have shown to be crucial in finding the key frequencies of the unactuated flow.
- Based on modal analysis results, three different actuation frequencies have been chosen to actuate the flow.
- An optimal actuation frequency has been found, ($F^+ = 3$). This gives a notable reduction of drag by 50%.

acknowledgements

This work is funded by the Swedish Energy Agency and supported by Volvo Trucks. Software licenses were provided by AVL List GMBH. Computations were performed at SNIC (the Swedish National Infrastructure for Computing) at the National Supercomputer Center (NSC) at LiU.

References

[1] M. Pastoor, L. Henning, B. R. Noack, R. King, and G. Tadmor, "Feedback shear layer control for bluff body drag reduction," *Journal of Fluid Mechanics*, vol. 608, pp. 161–196, 2008.
[2] D. J. Parkin, M. C. Thompson, and J. Sheridan, "Numerical analysis of bluff body wakes under periodic open-loop control," *Journal of Fluid Mechanics*, vol. 739, pp. 94–123, dec 2013.
[3] M. Gad-el Hak, "Introduction to flow control," *Flow Control*, no. 1904, pp. 1–107, 1998.
[4] S. L. Brunton and B. R. Noack, "Closed-Loop Turbulence Control: Progress and Challenges," *Applied Mechanics Reviews*, vol. 67, no. 5, p. 050801, 2015.
[5] G. Minelli, S. Krajnovi, and B. Basara, "Actuation of the flow field around a frontstep with a rounded leading edge," in *8th International Symposium Turbulence, Heat and Mass Transfer*, (Sarajevo, Bosnia and Herzegovina), 2015.
[6] S. Krajnović, R. Lárusson, and B. Basara, "Superiority of PANS compared to LES in predicting a rudimentary landing gear flow with affordable meshes," *International Journal of Heat and Fluid Flow*, vol. 37, pp. 109–122, oct 2012.
[7] S. Krajnović, G. Minelli, and B. Basara, "Partially-averaged Navier-Stokes simulations of two bluff body flows," *Applied Mathematics and Computation*, vol. 000, pp. 1–15, 2015.
[8] S. Krajnović, G. Minelli, and B. Basara, "Partially-Averaged Navier-Stokes Simulations of Flows Around Generic Vehicle at Yaw," *SAE Technical Paper*, 2016.
[9] S. S. Girimaji, "Partially-Averaged Navier-Stokes Model for Turbulence: A Reynolds-Averaged Navier-Stokes to Direct Numerical Simulation Bridging Method," *Journal of Applied Mechanics*, vol. 73, no. 3, p. 413, 2006.
[10] M. Germano, "Turbulence: the filtering approach," *Journal of Fluid Mechanics*, vol. 238, pp. 325–336, 1992.
[11] J. M. Ma, S. H. Peng, L. Davidson, and F. J. Wang, "A low Reynolds number variant of partially-averaged Navier-Stokes model for turbulence," *International Journal of Heat and Fluid Flow*, vol. 32, no. 3, pp. 652–669, 2011.
[12] B. Basara, S. Krajnović, and S. Girimaji, "PANS methodology applied to elliptic-relaxation based eddy viscosity transport model," *Turbulence and Interactions*, pp. 63–69, 2010.
[13] B. Basara, S. Krajnovic, S. Girimaji, and Z. Pavlovic, "Near-Wall Formulation of the Partially Averaged Navier Stokes Turbulence Model," *AIAA Journal*, vol. 49, pp. 2627–2636, dec 2011.
[14] S. Girimaji and K. Abdol-Hamid, "Partially Averaged NavierâĂŞStokes Model for Turbulence: Implementation and Validation," *AIAA paper*, no. January, 2005.
[15] AVL 2010, "AVL Fire manual, v2010," vol. Edition 11, 2010.
[16] U. Piomelli and J. Chasnov, *LARGE-EDDY SIMULATIONS: THEORY AND APPLICATIONS*. Kluwer Academic Publisher, 1996.
[17] J. L. Lumley, *Stochastic Tools in Turbulence - Applied Mathematics and Mechanics*, vol. 12. New York: Academic Press, 1970.